

This is the accepted manuscript made available via CHORUS. The article has been published as:

## Tailoring thermal emission via Q matching of photonic crystal resonances

M. Ghebrebrhan, P. Bermel, Y. X. Yeng, I. Celanovic, M. Soljačić, and J. D. Joannopoulos

Phys. Rev. A **83**, 033810 — Published 9 March 2011

DOI: [10.1103/PhysRevA.83.033810](https://doi.org/10.1103/PhysRevA.83.033810)

# Tailoring thermal emission via $Q$ -matching of photonic crystal resonances

M. Ghebrebrhan,<sup>1,\*</sup> P. Bermel,<sup>2,3,4</sup> Y. X. Yeng,<sup>5</sup> I. Celanovic,<sup>4</sup> M. Soljačić,<sup>1,4</sup> and J. D. Joannopoulos<sup>1,4</sup>

<sup>1</sup>*Department of Physics, Massachusetts Institute of Technology, Cambridge, Massachusetts 02139*

<sup>2</sup>*Center for Material Science and Engineering, Massachusetts Institute of Technology, Cambridge, Massachusetts 02139*

<sup>3</sup>*Research Laboratory of Electronics, Massachusetts Institute of Technology, Cambridge, Massachusetts 02139*

<sup>4</sup>*Institute for Soldier Nanotechnologies, Massachusetts Institute of Technology, Cambridge, Massachusetts 02139*

<sup>5</sup>*Department of Electrical Engineering and Computer Science,  
Massachusetts Institute of Technology, Cambridge, Massachusetts 02139*

We develop a model for predicting the thermal emission spectrum of a 2D metallic photonic crystal for arbitrary angles based on coupled-mode theory. Calculating the appropriate coupled-mode parameters over a range of geometrical parameters allows one to tailor the emissivity spectrum to a specific application. As an example, we design an emitter with a step-function cutoff suppressing long-wavelength emission, which is necessary for high-efficiency thermophotovoltaic systems. We also confirm the accuracy of the results of our model with finite-difference time-domain simulations.

PACS numbers: 42.70.Qs, 44.40.+a

## I. INTRODUCTION

The spectral emissivity of a blackbody is the upper limit that any material can achieve. However, in certain applications it is desirable to have an emitter that radiates only within a certain frequency bandwidth, a selective emitter. Photonic crystals, metallo-dielectric structures with periodic wavelength-scale refractive index modulations, are well-suited for creating a selective emitter by virtue of possessing photonic bandgaps [1–5]. Using metals introduces more flexibility in creating a selective emitter; below the plasma frequency of the metal, electromagnetic fields are strongly attenuated [6, 7], which assists broadband frequency selectivity [6–14]. However, the high infrared reflectivity of metals implies via Kirchhoff’s law, a low emissivity [15] and therefore requires a modification of the surface, by a 1D array of grooves [8] or a 2D array of holes [9–11, 14], to enhance emission at those frequencies. The surface periodicity allows light to couple to grazing, diffracted plane waves or surface plasmons, if they are present. Moreover if the grooves or holes are large enough they will support waveguide resonances that couple to one another providing another mechanism for enhancing thermal emission by increasing the interaction time of light with the material. While previous work [8–10, 14] has demonstrated that the peaks due to waveguide resonances occur at frequencies corresponding to the isolated waveguide resonant frequencies, the mechanism and quantitative prediction for the amplitude of the peaks were missing. Here we show that matching the radiative and absorptive rate of the photonic crystal resonances dictates the emissivity spectrum, and by tuning a small number of geometrical parameters, tailoring a broadband, selective thermal emitter becomes possible.

In particular, one such application of a selective broad-

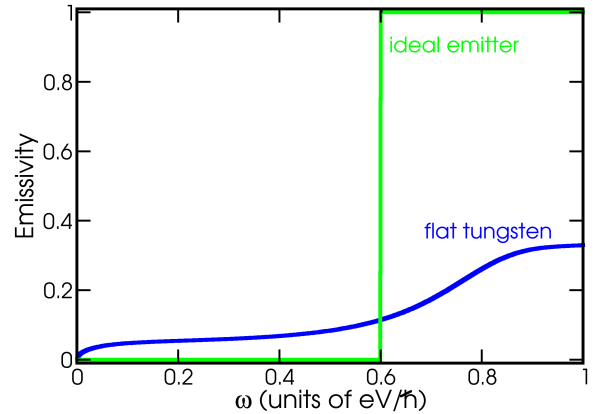


FIG. 1: Emissivity spectrum of flat, bulk tungsten (blue) and an ideal selective emitter (green) designed to match the 0.6 eV/ħ bandgap of InGaAs.

band emitter is in thermophotovoltaics (TPV). In TPV, the emitter, such as a slab of tungsten, is heated to a high temperature, radiating the majority of its energy in the infrared and onto a photovoltaic (PV) cell with a bandgap designed to lie in the infrared [16, 17]. InGaAs, for example, possesses a bandgap of 0.6 eV/ħ [10, 18]. However, low efficiency and power density are obtained since the typical greybody has low emissivity in the infrared; this is remedied with the selective emitter.

## II. LOSS RATES OF WAVEGUIDE RESONANCES

Consider the emissivity spectra illustrated in Fig. 1. The ideal selective emitter should only emit photons above a cutoff frequency. Here, the cutoff frequency cor-

---

\*Electronic address: mghebre@mit.edu

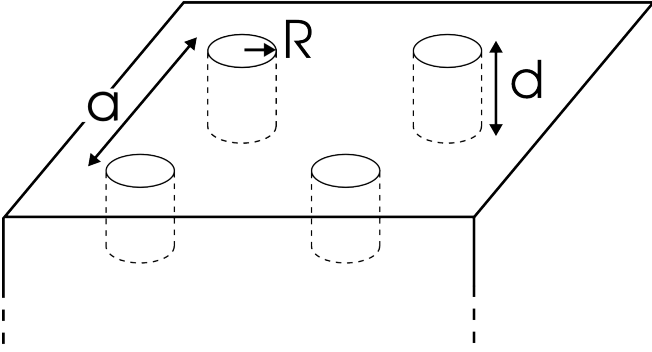


FIG. 2: A periodic array of cylindrical holes with period  $a$ , depth  $d$ , and radius  $R$  etched into a slab of tungsten. The hole depth is less than the tungsten slab thickness.

responds to the electronic bandgap of InGaAs. Tungsten, which has a high melting point and low emissivity beyond the cutoff frequency, is far from an ideal selective emitter. However, the introduction of a periodic array of holes, illustrated in Fig. 2, can greatly improve its selectivity via the creation of extra states on the surface that couple to external radiation.

Intuitively the radiative and absorptive rates of these coupled waveguide resonances should depend more strongly on the hole radius  $R$  and depth  $d$  than on the period  $a$ , therefore consider first a single, isolated hole ( $a \rightarrow \infty$ ). Because the field can penetrate into tungsten, the resonant mode within an isolated hole will be a linear combination of HE and EH-like modes. Only resonances with angular number  $\nu = 1$  will be considered since only those resonances in a periodic array of holes couple to plane waves at normal incidence. In addition, for the  $R$  and  $d$  values considered here for  $Q$ -matching,  $\nu = 1$  yields the lowest resonances. The hole resonances experience three types of losses: radiation through the top, absorption on the side walls and bottom, and absorption on the front tungsten surface. Since the last mechanism is a second-order effect dependent on the radiative rate, it is neglected. If the two remaining loss rates are not too large compared to the resonant frequency, then each can be calculated in the absence of the other [19]. From each loss rate a quality factor  $Q = \omega_o \tau / 2$  is calculated, where  $\omega_o$  is the resonant mode frequency and  $\tau$  is the lifetime (or inverse loss rate) associated with a particular loss mechanism. The quality factor is a dimensionless lifetime: after  $Q$  periods a resonance decays by  $\exp(-2\pi)$ . When these two loss rates are equal—the  $Q$ -matching condition, complete absorption of incident radiation occurs.

The loss rate due to absorption can be closely approximated by closing the top with a perfectly conducting metal. A perfect magnetic conductor cover, corresponding to an electric field maximum at the opening, could just as well be employed since the absorptive rate does not depend much on which boundary condition is used. Finite-

difference time-domain (FDTD) simulation is used to simulate the closed hole [20, 21]. A point source is placed in the cavity, and resonant modes are excited whose loss rates are extracted by a filter-diagonalization method [22]. The resonant frequency  $\omega_o a / 2\pi c$  and absorptive quality factor  $Q_{\text{abs}} = \omega_o \tau_{\text{abs}} / 2$  are plotted in Fig. 3(a) and Fig. 3(b) as functions of the cavity radius and depth for the first three hole resonances. The general trend of  $Q_{\text{abs}}$  decreasing towards the left can be understood from an equivalent definition of  $Q$ ,  $Q_{\text{abs}} = \omega_o U / P_{\text{abs}}$ . Decreasing the hole volume reduces the total field energy  $U$  of the mode and forces a larger value of the electric field on the tungsten surface thereby raising  $P_{\text{abs}}$ .

The radiative quality factor  $Q_{\text{rad}} = \omega_o \tau_{\text{rad}} / 2$ , plotted in Fig. 3(c) as a function of  $R$  and  $d$ , is obtained by replacing tungsten with a perfect conductor in simulations. The lack of an intrinsic length scale implies that  $Q_{\text{rad}}$  will depend only on the ratio  $d/R$  and is manifested in Fig. 3(c) as lines emanating from the origin. It can be shown to leading order in  $d/R$  that

$$Q_{\text{rad}} \propto \left(\frac{d}{R}\right)^3 \quad (1)$$

through  $Q_{\text{rad}} = \omega_o U / P_{\text{rad}}$ . The stored field energy

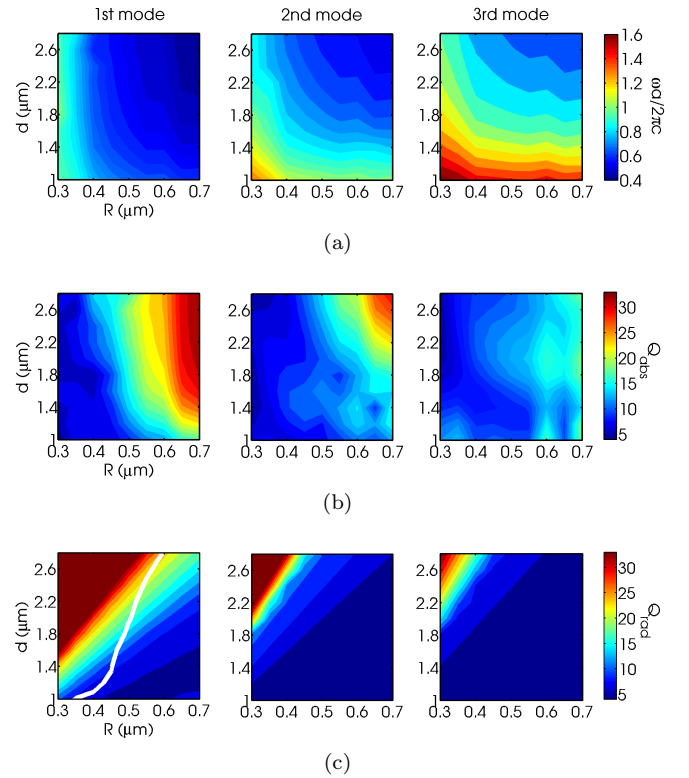


FIG. 3: (a) Resonant mode frequency in units of  $2\pi c/a$  with  $a = 1 \mu\text{m}$ , (b)  $Q_{\text{abs}}$ , and (c)  $Q_{\text{rad}}$  of the lowest three modes. The absorptive and radiative  $Q$  are plotted on the same color scale.  $Q$ -matching of the first resonance is indicated by the white line.

is approximately the product of the hole volume and the electric field intensity at the hole center,  $U \approx \epsilon_0 R^2 d |\mathbf{E}_{\text{center}}|^2$ . The radiated power is the product of the Poynting field at the cavity opening and the area of the opening,  $P_{\text{rad}} \approx R^2 |\mathbf{E}_{\text{opening}}|^2 / (c\mu_0)$ . From numerical simulations of holes with  $R$  and  $d$  varied separately one obtains  $|\mathbf{E}_{\text{opening}}|/|\mathbf{E}_{\text{center}}| \approx 2R/d$ , which gives  $Q_{\text{rad}} \propto \omega_o d^3 / (cR^2)$ . Expressing the resonant frequency  $\omega_o$  in terms of the geometric parameters yields the desired result to leading order in  $d/R$ . FDTD simulations confirm Eq. 1, but with an exponent slightly less than 3.

$Q$ -matching is attained wherever the two surfaces,  $Q_{\text{abs}}(R, d)$  and  $Q_{\text{rad}}(R, d)$ , intersect. For the first resonance this occurs on the white line in Fig. 3(c). Above the line  $Q_{\text{rad}}$  is too large, the hole is under-coupled to external radiation. Below it  $Q_{\text{rad}}$  is too small and the hole is over-coupled to external radiation, power can effectively couple into the hole, but it's trapped for too short a time to be absorbed. Critical coupling is achieved by tuning the radius to increase  $Q_{\text{rad}}$  to a high enough value.

### III. EFFECT OF PERIOD

The optimal dimensions for a periodic array of holes may not be the same as for an isolated hole. Since the far field of neighboring holes can destructively interfere  $Q_{\text{rad}}$  may increase. Moreover,  $Q$ -matching has been achieved for spherical waves converging onto the hole. The period's effect on  $Q_{\text{rad}}$  can be determined through a field-matching formalism described in Ref. 23. In this formalism, the field above the perfect conductor slab is expanded in a plane wave basis, the field inside the holes is expanded as a linear combination of waveguide modes, and boundary conditions are imposed to produce a set of linear equations for the field amplitudes. It is found that  $Q_{\text{rad}}$  is typically larger than that of an isolated hole due to partial, destructive interference of the far field. The period can change  $Q_{\text{rad}}$  by about 50% relative to the isolated hole  $Q_{\text{rad}}$ . Most of the variation in  $Q_{\text{rad}}$  occurs near periods where there exists diffracted plane waves that are resonant with a waveguide mode. During this resonance it is possible for  $Q_{\text{rad}}$  to be less than that of the isolated hole value.  $Q_{\text{abs}}$ , on the other hand, is not expected to change by more than a few percent for holes that are separated by a skin depth or more since that coupling is exponentially dependent on the separation [24]. Nonetheless, the  $Q$ -matching condition of the isolated holes can serve as a guide towards the optimal hole parameters for the photonic crystal slab.

Using the previously built intuition we simulate a tungsten photonic crystal with hole dimensions predicted to satisfy  $Q$ -matching:  $R = 0.5 \mu\text{m}$ ,  $d = 1.89 \mu\text{m}$ , and period  $a = 4.8 \mu\text{m}$ . A normally incident, linearly polarized plane wave is directed at the tungsten photonic crystal slab. Perfectly matched layers (PML) terminate the computational cell above the slab and periodic boundary con-

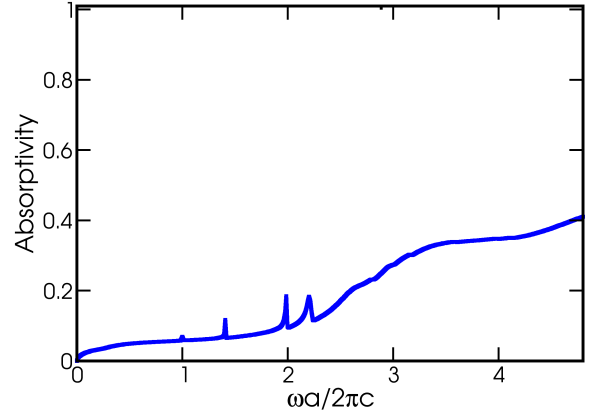


FIG. 4: Absorption spectrum for the tungsten photonic crystal slab with  $a = 4.8 \mu\text{m}$ ,  $R = 0.104a$ , and  $d = 0.394a$ . Diffraction appears as sharp peaks and resonant peaks due to photonic crystal modes appear at approximately  $2.7$  and  $3.4 \ 2\pi c/a$ .

dition ( $\mathbf{k}_{\parallel} = (k_x, k_y) = 0$ ) on the sides. (PML is unnecessary below since the slab is opaque to radiation.) The absorptivity spectrum is calculated from the reflectivity spectrum  $A(\omega) = 1 - R(\omega)$ . The emissivity spectrum, for normal emission, is obtained from the absorptivity spectrum via Kirchhoff's law which states that for a body in thermal equilibrium, emissivity and absorptivity must match at each frequency, wave vector, and polarization [15, 25, 26]. Due to the large period, the emissivity spectrum of the  $a = 4.8 \mu\text{m}$  crystal, Fig. 4, is essentially that of flat tungsten with sharp peaks due to grazing plane waves or Bragg-diffracted surface plasmons and broadened photonic crystal resonances superimposed. Because

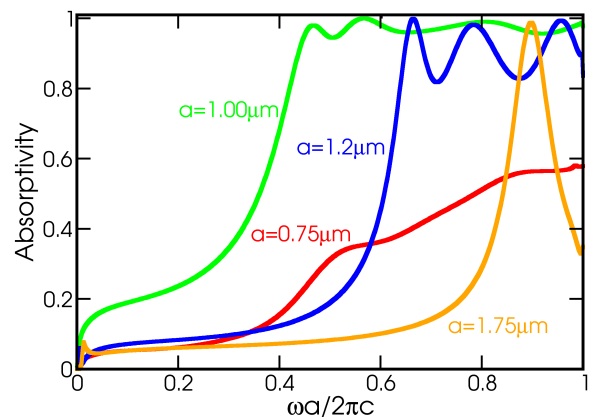


FIG. 5: Absorption spectra for photonic crystal slabs with various  $a$  but  $R$  and  $d$  fixed at  $0.5$  and  $1.89 \mu\text{m}$ , respectively.

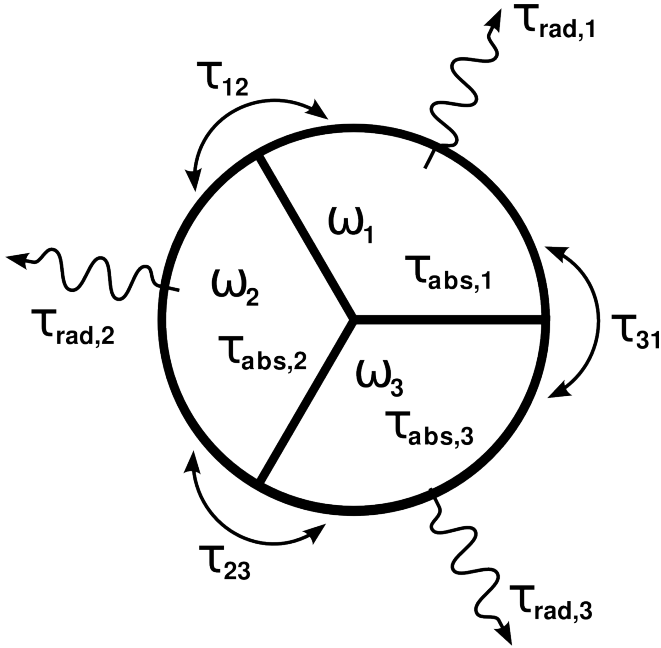


FIG. 6: A multimode resonator with resonant frequencies  $\omega_i$ , absorptive and radiative lifetimes  $\tau_{\text{abs},i}$  and  $\tau_{\text{rad},i}$ , respectively. Resonances radiatively couple to each other with rate  $1/\tau_{ij}$ .

the holes occupy a small fraction of the surface, coupling into the photonic crystal resonances from normal incidence is weak. (However,  $Q_{\text{rad}}$  of the first isolated hole and photonic crystal resonance is 14.3 and 12.7, respectively.) To realize a stronger frequency selectivity it is necessary to adjust  $a$ ; plotted in Fig. 5 are the emissivity spectra for various  $a$ . As  $a$  is decreased, the first resonant peak eventually appears below the diffraction limit,  $\omega a/2\pi c = 1$ . Further reduction of  $a$  pushes the diffraction limit above additional resonances, increasing the bandwidth of the high emissivity region. This can be continued up to  $a = 2R$  at which point the hole resonances are strongly coupled to each other through the tungsten side walls in addition to the nonradiative coupling via evanescent plane waves. Clearly for small enough periods, such as for  $a = 0.75 \mu\text{m}$ , the photonic crystal resonances can no longer be described as coupled waveguide resonances. Note that at wavelengths much larger than  $a$ , different absorptivities occur due to the varying ratios of air hole to tungsten side wall volumes. In the long wavelength limit the free electron density makes the dominant contribution to the permittivity and effective medium theory is valid. Decreasing the tungsten fraction decreases the free electron density. This lowers the effective plasma frequency which increases the absorption rate.

#### IV. COUPLED-MODE THEORY

We now focus on the  $a = 1.2 \mu\text{m}$  emissivity spectrum below the diffraction limit and understand it through temporal coupled-mode theory [27–29]. The tungsten photonic crystal can be thought of as a multimode resonator, illustrated in Fig. 6, with only three resonances below the diffraction limit. Associated with each resonance is a resonant frequency  $\omega_i$ , absorptive lifetime  $\tau_{\text{abs},i}$ , radiative lifetime  $\tau_{\text{rad},i}$ . In addition they can radiatively couple to each other with a lifetime  $\tau_{ij}$  ( $i \neq j$ ) on the order of  $\tau_{\text{rad},i}$  [30]. The coupled-mode equations for the multimode resonator are,

$$\frac{d\mathbf{a}}{dt} = (i\Omega_0 - \Gamma)\mathbf{a} + D^T s_+ \quad (2)$$

$$s_- = Cs_+ + D\mathbf{a}, \quad (3)$$

where  $\mathbf{a}$  is a three-component vector describing the resonant mode amplitudes,  $\Omega_0$  is a  $3 \times 3$  diagonal matrix of the resonant mode frequencies,  $\Gamma$  is a  $3 \times 3$  matrix of decay rates,  $s_{\pm}$  are the incoming/outgoing channel amplitudes,  $C$  is the direct pathway scattering amplitude, and  $D$  is  $1 \times 3$  matrix of the resonance-channel coupling amplitudes. The reflectivity is  $R = |s_-/s_+|^2$ . The decay rate matrix  $\Gamma$  can be separated into a radiative contribution  $\Gamma_r$  and an absorptive contribution  $\Gamma_a$  with  $\Gamma_{r,ii} = 1/\tau_{\text{rad},i}$  and  $\Gamma_{a,ii} = 1/\tau_{\text{abs},i}$ . The resonance-resonance coupling rates,  $1/\tau_{ij}$ , are given by the off-diagonal part of  $\Gamma_r$  which are dependent on the radiative rates  $\Gamma_{r,ii}$ . The dependence comes about through the matrix constraint  $2\Gamma_r = D^\dagger D$ , which is a consequence of energy conservation and reciprocity. In addition, the direct pathway scattering matrix constrains the phases of  $D$  via the relation  $CD^* = -D$ . Since the front surface absorption is neglected, the front surface is approximated as a perfect

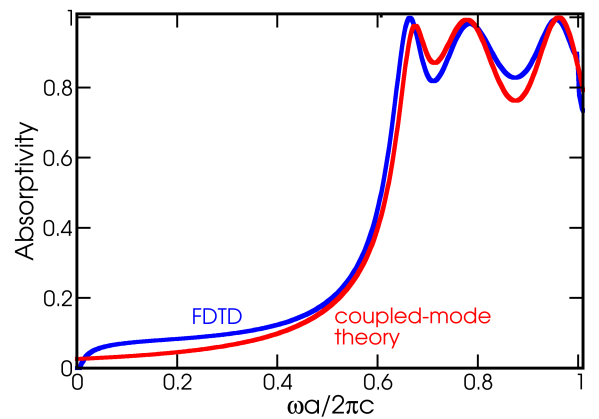


FIG. 7: Absorptivity spectrum for  $a = 1.2 \mu\text{m}$  calculated via FDTD simulation (blue) and coupled-mode theory (red).

conductor and  $C$  is set to  $-1$ . The phase of the elements of  $D$  depend in part on how many ways the photonic crystal resonances can couple to each other [30]. For instance, in the case of hole depth equal to slab thickness, the photonic crystal resonances couple via the top and bottom openings. If the resonances have with opposite parity, then the resonances will not couple, i.e.,  $\tau_{ij} \rightarrow \infty$ . Here, the hole depth is less than the slab thickness by more than a couple skin depths eliminating one of the channels, and so all resonances will radiatively couple to one another. This also implies that the resonance-channel coupling amplitudes will have the same phase.

From FDTD simulations we obtain  $\omega_i$ ,  $\tau_{\text{abs},i}$ , and  $\tau_{\text{rad},i}$  for each resonance. In particular,  $\tau_{\text{rad},i}$  is obtained from simulating a unit cell of the photonic crystal with the radius widened by a skin depth. The resulting emissivity spectrum is compared with the emissivity spectrum obtained from the full FDTD simulation in Fig. 7. Since coupled-mode theory is a perturbation theory, it is most accurate for resonances with total  $Q \gg 1$ ; here the resonances have total  $Q$  of 8.0, 4.4, and 6.3, respectively, and unsurprisingly, the spectra display some differences. The resonances above the diffraction limit are not taken into account, doing so requires not only their resonant frequencies and lifetimes, but also modifying the coupled-mode equations to include the extra channels that correspond to diffracted plane waves. Accounting for the first order diffraction at normal emission would in general require  $s_{\pm}$  to be a  $10 \times 1$  vector (a channel for s- and p-polarization at each reciprocal wavevector),  $D$  a  $10 \times 3$  matrix, and  $C$  a  $10 \times 10$  frequency-dependent matrix. For frequencies much less than the cut-off frequency where the absorption is due primarily to the front surface of tungsten the coupled-mode equations here will not work. In principle it can be accounted for in the coupled-mode equations by considering the front surface absorption as another channel [30]. Since the absorptivity spectrum is accurately reproduced with only the coupled-waveguide resonances, surface plasmons due to tungsten's permittivity can apparently be ignored. Surface plasmon resonances for flat tungsten would appear at a frequency just under the diffraction threshold; at least for shallow holes (corresponding to  $d/a < 0.1$  in Ref. 4, 31), this remains true. However, this portion of the absorption spectrum is well-reproduced with the coupled-waveguide resonances whose decay rates are matched. In cases where surface plasmons are important, they could be included into the coupled-mode equations once their decay rates are known.

Off-normal emission ( $\mathbf{k}_{\parallel} \neq 0$ ) can be handled with this framework as well. The absorptive  $Q$  will not change much with  $\mathbf{k}_{\parallel}$  as long as the holes are separated by at least a few skin depths [24]. The mode-matching formalism described earlier can be used to obtain the resonant frequency and radiative  $Q$  for non-zero  $\mathbf{k}_{\parallel}$ . It is found that the resonant frequency changes little with  $\mathbf{k}_{\parallel}$ ; this reflects the fact that the resonant peaks are due to coupled hole resonances. The emissivity spectrum calculated

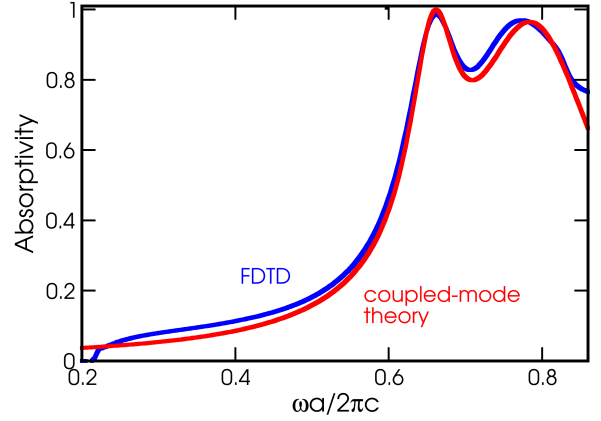


FIG. 8: Absorptivity spectrum for the same structure as in Fig. 7, but with  $\mathbf{k}_{\parallel}a/2\pi = (0.1776, 0.1056)$ . Peaks in the emissivity would correspond to polar angles of 18 and 15° and azimuthal angle of 31°.

by FDTD and coupled-mode theory for an arbitrary  $\mathbf{k}_{\parallel}$  is plotted in Fig. 8. It should be noted that the normal and off-normal spectra display little difference, in particular the first and second resonances retain nearly perfect emissivity at polar angles of 18 and 15°, respectively. This high selectivity continues nearly unchanged up to the diffraction threshold where new channels open and the radiative  $Q$  drops in value. Once the diffraction threshold is crossed it's necessary to solve the coupled-mode equations again. The direct-pathway scattering matrix  $C$  can be obtained from the formalism of Ref. 23 by reducing the depth of holes to eliminate the resonances. The square of the magnitudes of the elements of  $D$  can be obtained from the fraction of power radiated by each resonance into each channel and the radiative  $Q$ . Finally, the phases of the elements of  $D$  can be obtained from solving the equation  $CD^* = -D$ .

## V. APPLICATIONS AND CONCLUSIONS

Demonstrating that it is possible to predict the emissivity spectra with only a few input parameters— the optical constants of tungsten,  $a$ ,  $R$ , and  $d$ , attention can be directed towards applications. In TPV and solar TPV (STPV), the radiated photons from a high temperature radiator are captured and converted into electron-hole pairs via a photovoltaic cell [16, 17]. In the case of STPV, concentrated sunlight is used to heat the tandem absorber-emitter structure which then radiates onto a photovoltaic cell [32, 33]. In both cases, the emitter is heated to over 1000 K. The selective emitter described here can dramatically improve both the efficiency and power density of the TPV/STPV system by enhancing

the emission of above bandgap energy photons that directly generate electron-hole pairs in the PV cell, and suppressing emission of low-energy photons that would only heat the photovoltaic cell. Evidently, Fig. 8 shows that this remains true even for large polar angles. Moreover retaining the low-energy photons contribute toward keeping the emitter hot [34]. One such realistic structure would be the tungsten photonic crystal in Figs. 7 and 8 which has a cutoff frequency of  $0.67\text{ eV}/\hbar$ . It can be made to better match the  $0.6\text{ eV}/\hbar$  bandgap of InGaAs [18] by slightly widening the holes.

In conclusion we have demonstrated how  $Q$ -matching, via the geometrical parameters, can be used to tailor the emissivity spectrum of 2D metallic photonic crystals. One advantage of this approach compared to FDTD or finite-element methods is that the emissivity spectra can be calculated much more quickly. This becomes important when one considers that thermal radiation is incoherent, and the emissivity at all  $\mathbf{k}_{\parallel}$  is needed. Once the

reflectivity spectrum as a function of frequency, polarization, and  $\mathbf{k}_{\parallel}$  is obtained, the radiated power at a given temperature can be obtained by averaging the emissivities over polarization, weighing by the Planck distribution, and integrating over  $\mathbf{k}_{\parallel}$  and frequency.

### Acknowledgements

The authors would like to thank S. G. Johnson and J. Bravo-Abad for useful discussions. This work was supported in part by the Materials Research Science and Engineering Center Program of the National Science Foundation under Grant No. DMR 0819762, the MIT S3TEC Energy Research Frontier Center of the Department of Energy under Grant No. DESC0001299, and the Army Research Office through the Institute for Soldier Nanotechnologies under Contract No. DAAD-19-02-D0002.

- 
- [1] E. Yablonovitch, Phys. Rev. Lett. **58**, 2059 (1987).
  - [2] S. John, Phys. Rev. Lett. **58**, 2486 (1987).
  - [3] J. D. Joannopoulos, S. G. Johnson, J. N. Winn, and R. D. Meade, *Photonic Crystals: Molding the Flow of Light* (Princeton Univ. Press, 2008), 2nd ed.
  - [4] J.-J. Greffet, R. Carminati, K. Joulain, J.-P. Mulet, S. Mainguy, and Y. Chen, Nature **416**, 62 (2002).
  - [5] M. Laroche, R. Carminati, and J. J. Greffet, Phys. Rev. Lett. **96**, 123903 (2006).
  - [6] D. R. Smith, S. Schultz, N. Kroll, M. S. K. M. Ho, and C. M. Soukoulis, Appl. Phys. Lett. **65**, 645 (1994).
  - [7] E. R. Brown and O. B. McMahon, Appl. Phys. Lett. **67**, 2138 (1995).
  - [8] D. L. C. Chan, M. Soljacic, and J. D. Joannopoulos, Phys. Rev. E **74**, 016609 (2006).
  - [9] D. L. C. Chan, M. Soljacic, and J. D. Joannopoulos, Opt. Express **14**, 8785 (2006).
  - [10] H. Sai and H. Yugami, Appl. Phys. Lett. **85**, 3399 (2004).
  - [11] A. Heinzl, V. Boerner, A. Gombert, B. Blasi, V. Wittwer, and J. Luther, Journal of Modern Optics **47**, 2399 (2000).
  - [12] H. Sai, Y. Kanamori, K. Hane, H. Yugami, and M. Yamaguchi, IEEE pp. 762–765 (2005).
  - [13] S.-Y. Lin, J. G. Fleming, and I. El-Kady, Appl. Phys. Lett. **83**, 593 (2003).
  - [14] I. Celanovic, N. Jovanovic, and J. Kassakian, Appl. Phys. Lett. **92**, 193101 (2008).
  - [15] F. Reif, *Fundamentals of Statistical and Thermal Physics* (McGraw-Hill, 1965).
  - [16] H. H. Kolm, Quarterly Progress Report, Group 35, MIT Lincoln Laboratory (1953).
  - [17] B. Wedlock, Proc. IEEE **51**, 694 (1963).
  - [18] M. W. Dashiell, J. F. Beausang, H. Ehsani, G. J. Nichols, D. M. Depoy, L. R. Danielson, P. Talamo, K. D. Rahner, E. J. Brown, S. R. Burger, et al., IEEE Transactions on Electron. Devices **53**, 2879 (2006).
  - [19] H. A. Haus, *Waves and Fields in Optoelectronics* (Prentice-Hall, New Jersey, 1984).
  - [20] A. Taflov and S. C. Hagness, *Computational Electrodynamics: The Finite-Difference Time-Domain Method* (Artech, Norwood, MA, 2000).
  - [21] A. F. Oskooi, D. Roundy, M. Ibanescu, P. Bermel, J. D. Joannopoulos, and S. G. Johnson, Comp. Phys. Comm. **181**, 687 (2010).
  - [22] V. A. Mandelshtam and H. S. Taylor, J. Chem. Phys. **107**, 6756 (1997).
  - [23] J. Bravo-Abad, F. J. Garcia-Vidal, and L. Martin-Moreno, Phys. Rev. Lett. **93**, 227401 (2004).
  - [24] A. Yariv, Y. Xu, R. K. Lee, and A. Scherer, Opt. Lett. **24**, 711 (1999).
  - [25] C. Luo, A. Narayanaswamy, G. Chen, and J. D. Joannopoulos, Phys. Rev. Lett. **93**, 213905 (2004).
  - [26] D. L. C. Chan, M. Soljacic, and J. D. Joannopoulos, Phys. Rev. E **74**, 036615 (2006).
  - [27] S. Fan and J. D. Joannopoulos, Phys. Rev. B **65**, 235112 (2002).
  - [28] S. Fan, W. Suh, and J. D. Joannopoulos, J. Opt. Soc. Am. A **20**, 569 (2003).
  - [29] D. L. C. Chan, I. Celanovic, J. D. Joannopoulos, and M. Soljacic, Phys. Rev. A **74**, 064901 (2006).
  - [30] W. Suh, Z. Wang, and S. Fan, IEEE J. Quantum Electron. **40**, 1511 (2004).
  - [31] W. L. Barnes, T. W. Preist, S. C. Kitson, and J. R. Sambles, Phys. Rev. B **54**, 6227 (1996).
  - [32] R. Swanson, Proc. IEEE **67**, 446 (1979).
  - [33] W. Spirkel and H. Ries, J. Appl. Phys. **57**, 4409 (1985).
  - [34] Y.-S. Kim, S.-Y. Lin, A. S. P. Chang, J.-H. Lee, and K.-M. Ho, J. Appl. Phys. **102**, 063107 (2007).